Design and Optimization Method for Hypersonic Quasi-Waverider

Wen Liu,* Chen-An Zhang,† and Fa-Min Wang‡
Institute of Mechanics, Chinese Academy of Sciences, 100190 Beijing, People's Republic of China
and
Zheng-Yin Ye§
Northwestern Polytechnical University, 710072 Xi'an, People's Republic of China

The waverider has an extensive application prospect in the design of hypersonic vehicles due to its excellent aerodynamic efficiency. However, it is known that the original cone-derived waverider is longitudinally unstable. To solve the problem, a design method for hypersonic quasi-waverider configuration is first proposed and then a genetic algorithm optimization framework is constructed to obtain optimum quasi-waveriders with different constraints. During the optimization, the aerodynamic performance is evaluated by an efficient aerodynamic model that considers the impacts of strong viscous interaction effects. Results from numerical simulations show that, for the optimum quasi-waveriders without constraints, good shock wave attachment along the leading edge is achieved, and the maximum lift-to-drag ratio (L/D) is even higher than that of the original waverider. Optimized quasi-waveriders are also generated based on the constraints of volumetric efficiency and stability. The L/D first increases and then decreases with the increase in volumetric efficiency. In addition, an interesting phenomenon is found that the L/D is reduced almost linearly with the increase in the degree of stability at each design condition. Furthermore, a linear relationship is also constructed between the variation of L/D with respect to degree of stability and the viscous interaction parameter $\bar{V}'$.

Nomenclature

a_i	=	coefficient of base function
b_i	=	power of the curve equation
C_D	=	drag coefficient
$C_{D\mathrm{fric}}$	=	friction drag coefficient
$C_{D\mathrm{wave}}$	=	wave drag coefficient
C_L	=	lift coefficient
C_m	=	pitching moment coefficient
C_N	=	normal force coefficient
ds	=	degree of stability
H	=	flight altitude
L	=	length of the waverider, 4 m
M_∞	=	Mach number
p	=	pressure
S_{lower}	=	surface area of the lower surface
S_{upper}	=	surface area of the upper surface
T	=	temperature
V	=	volume of the waverider
$\bar{V}'$	=	viscous interaction parameter
X_{ac}	=	aerodynamic-center location
X_{cp}	=	center-of-pressure location
x_{le}	=	X coordinate of the leading-edge point
y_{te}	=	height of the waverider at the symmetry plane
α	=	angle of attack
β	=	shock wave angle
γ	=	ratio of the specific heats, 1.4 for perfect gas
Δa_{max}	=	maximum relative variation of the design variables a_i during the optimization
δ_x^*	=	boundary-layer displacement thickness
θ	=	deflection angle of body surface relative to the free-stream direction
ρ	=	density

I. Introduction

HYPERSONIC flight is drawing more and more attention from researchers all over the world. Several past and ongoing programs have been executed to investigate the key technologies of hypersonic vehicles and advance the state-of-the-art in hypersonic aerodynamics, such as National Aerospace Plane [1], Force Application and Launch from Continental United States [2], and Hypersonic International Flight Research [3]. Various kinds of configurations are designed based on different mission requirements. A common challenge encountered by different hypersonic vehicles is how to obtain high lift-to-drag ratio (L/D). Higher L/D means larger down and cross range, which is usually a key driving parameter behind any vehicle design. However, the improvement of L/D is especially difficult due to the severe wave drag and friction drag at hypersonic flight conditions. In fact, according to a well-known survey by Kuchemann [4], a type of "L/D barrier" exists for traditional hypersonic vehicles.

To break the L/D barrier, the concept of waverider proposed by Nonweiler [5] came to renaissance in the 1980s. Differing from the flow physics around traditional hypersonic configurations, the shock wave is attached to the entire leading edge of the waverider at the design condition, thus preventing the leakage of high-pressure gas from the lower surface onto the upper surface and achieving excellent aerodynamic efficiency. Nevertheless, the L/D advantage of waverider was widely questioned at early stage by main concerns for hypersonic viscous flow effects, aerothermodynamic effects of the sharp leading edge, limited volumetric efficiency, and off-design performance. Such skepticism began to be eliminated gradually Since the concept of viscous optimized waverider was proposed by Bowcutt et al. [6] and Corda and Anderson [7], where the viscous effects were incorporated into the optimization process for the first time. The viscous optimized waveriders became the first hypersonic configurations to break the aforementioned L/D barrier. Since then, lots of researches have been carried out to help expand the applicability of waveriders to realistic aerospace missions. For example, various waverider design and optimization methods from different generating flowfield were developed to improve the volumetric efficiency, payload ability, and flexibility of the geometry [8–17];

several leading-edge blunting methods were studied to achieve a good balance between the aerodynamic and aerothermodynamic concerns [18,19]; off-design performance was evaluated from various aspects [20,21]. In addition, efforts on incorporation of the waveriders into different practical hypersonic vehicles were also made [22–25].

Despite the enriched researches mentioned above, one urgent topic for waveriders to be solved is the problem of longitudinal stability. Modern active control system makes it possible for the vehicles to be acceptably unstable at hypersonic conditions [26]. However, a good type of configuration should have the potential to flexibly change the stability margin during the aerodynamic design according to the overall performance requirements. Past researches have shown that the cone-derived waverider is statically unstable because the center of pressure is in front of the center of gravity when the latter is located at the center of volume [27]. In fact, in actual aircraft design, the center of gravity usually does not coincide with the center of volume and can be moved forward by appropriate adjustment of the payload position or using some ballast weight. Jia et al. [28] derived the variation trend of the center of pressure with angle of attack for different streamlines by applying the Newtonian theory on a simplified streamline model, which is introduced in detail in the Appendix. They have found that, for a concave streamline, the center of pressure moves forward monotonously as the angle of attack increases, whereas the trend is just opposite for a convex one. A sketch map of different curves and corresponding center of pressure is given in Fig. 1. A self-trimmed vehicle is generally preferred because no extra trim drag is produced by the elevator. To satisfy the trim requirement, the center of gravity should coincide with the center of pressure at the design angle of attack. Then a concave streamline would be statically unstable in that the center of pressure being in front of the center of gravity tends to produce a nose-up moment as the angle of attack increases. From this perspective, the idealized cone-derived waverider is statically unstable because the streamlines of the lower surface are concave.

Several design and optimization methods may be employed to improve the longitudinally static stability of the cone-derived waverider. First, the freestream upper surface can be disturbed to alter the center-of-pressure location. However, minor modification may only work at small angles of attack due to the expansion effects, whereas major modification may lead to large loss of L/D. Second, compared with the cone-derived waveriders, ones derived from the axisymmetric power-law body flows may exhibit better longitudinal stability because the streamlines are convex [29]. However, no analytical solutions exist for such base flows, and instead they are usually calculated using computational fluid dynamics (CFD) codes [29,30]. Then the process for choosing an optimum base flow according to different stability constraints may be time-consuming and complex. An initial study on this topic is given by Wang et al. [30]. Another alternative is to directly modify the original concave lower surface of cone-derived waveriders. In fact, affected by the strong viscous interactions at large Mach numbers and high altitudes, the effective shape would differ from the original shape apparently and reasonable modification of the lower

surface can even obtain a waverider with better aerodynamic performance [31]. Accordingly, appropriate deviation and optimization from an idealized waverider surface may be feasible.

Following the last idea mentioned above, a design and optimization method for hypersonic quasi-waverider configuration is proposed in this paper. First, the definition and generation process of the lower surface is introduced. Then the optimization by genetic algorithm (GA) is carried out, during which the volumetric efficiency, trim, and longitudinal stability (the location of center of pressure and aerodynamic center) can be taken into account. To improve the optimization efficiency, the aerodynamic performances are evaluated by an aerodynamic model that can consider the strong viscous interaction effects by a semi-empirical method. Finally, CFD is used to calculate the aerodynamic forces of the resulting optimum shapes with different constraints.

II. Definition of the Quasi-Waverider

The proposed configuration is named as "quasi-waverider" in that it can be generated from any original waverider by the following steps:

1) The leading edge of the original waverider is kept unchanged.

2) At a different longitudinal plane, the profile of the lower surface is determined by the same curve equation, started from the point at the leading edge and cutoff at the base plane. The curve equation is determined by the sum of a series of power law functions, whose coefficients are varied during the optimization according to different design objectives. In such ways, good uniformity of pressure distribution is expected and the flexibility of the geometry generation can also be improved greatly.

In fact, the profile curve of the lower surface can also be located along the circumferential direction just as the streamline of the waverider does. However, we find that no essential difference exists between the two methods and the obtained configurations have very close aerodynamic performances. Therefore, here the profile curve is located along the longitudinal plane for simplicity.

3) The height of the symmetry plane is kept the same as that of the original waverider or slight deviation from it, so that the shock wave position and volumetric efficiency is held not changed much.

4) Finally, the freestream upper surface is employed.

Later results will show that good shock wave attachment can be obtained for the quasi-waveriders. However, they cannot "ride" on the shock wave along the whole leading edge as perfectly as that of the original waverider. Then referring to the definition and difference of the steady flow, quasi-steady flow, and unsteady flow, the proposed configuration here is named as "quasi-waverider."

A. Determination of the Leading Edge

In practical engineering applications, the leading edge of any kind of waveriders can be used according to various design requirements. Referring to the idea of Bowcutt et al. [6], here the leading edge of a typical viscous optimized cone-derived waverider is employed. The
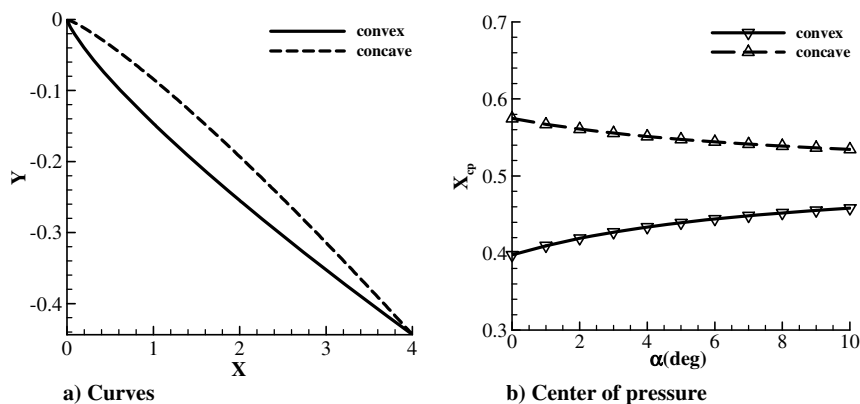

a) Curves   b) Center of pressure

Fig. 1   Sketch map of different curves and corresponding center of pressure.

Table 1   Design condition and geometric parameters used to define the waverider

H	M_∞	β	L
60 km	15	8.5 deg	4 m

detailed optimization process is introduced in Ref. [31]. The design condition and relevant parameters are listed in Table 1.

The waverider is determined by the base curve on the base plane shown in Fig. 2 and the generated viscous optimized waverider is shown in Fig. 3. The base curve on the left half ($Z \geq 0$), defined on the shock wave circle with a nondimensionalized radius of 0.149, can be expressed as the following third-order polynomial:

$$Y = -0.0687 - 6.36Z^2 + 24.12Z^3 \tag{1}$$

B.   Generation of the Lower Surface

To change the concavo-convex characteristics of the lower surface flexibly, here a series of power law functions are taken as the base functions and the profile curve can be determined as follows:

$$\frac{y}{L} = \sum_{i=1}^{11} a_i \left(\frac{x}{L}\right)^{b_i} \tag{2}$$

where a_i is the coefficient of the base function and $a_1 - a_{10}$ are the design variables; the power b_i is determined as $b_i = 0.5 + 0.1i(1 \leq i \leq 11)$. After the height of the quasi-waverider at the symmetry plane y_{te} and the values of control variables are given, a_{11} can be calculated as
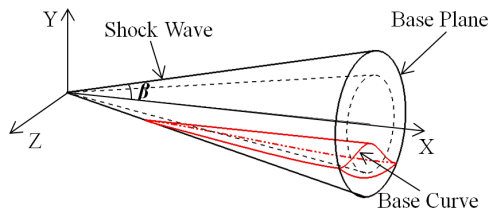
Fig. 2   Generation of cone-derived waverider.
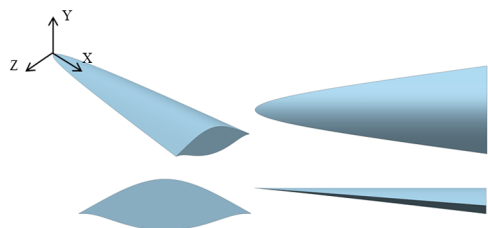
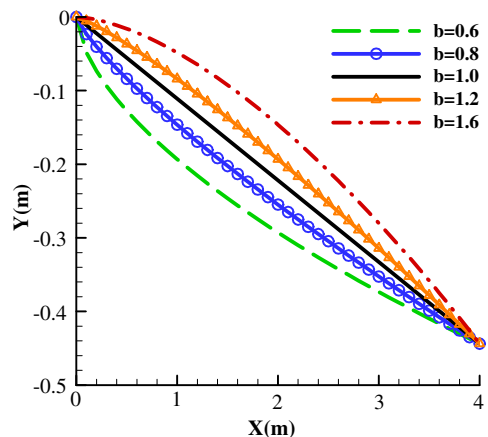**Fig. 3   Viscous optimized waverider.**

Fig. 4   Profile curves determined by different single base functions.

$$a_{11} = -\frac{y_{te}}{L} - \sum_{i=1}^{10} a_i \tag{3}$$

Here the height y_{te} is set to be the same as that of the original cone-derived waverider at the symmetry plane, which is equal to 0.44376 m.

According to the definition of the lower surface depicted above, the profile curve of the longitudinal cross section at any other position can be determined as

$$\frac{y}{L} = \sum_{i=1}^{11} a_i \left(\frac{x - x_{le}}{L}\right)^{b_i} \tag{4}$$

where x_{te} denotes the X coordinate of the leading-edge point at the corresponding cross section.

In practical applications, the number of design variables and the power b_i can be assigned flexibly based on the specified optimization problem. Generally, more control variables means more iterative steps and less efficient optimization process, but can produce more refined optimization results. Because the aerodynamic forces are calculated using an efficient aerodynamic model during the optimization, the time spent by more iterative steps is acceptable. Consequently, a total of 10 design variables are used for this problem.

Figure 4 describes the profile curves determined by different single base functions. It can be inferred that the geometry of lower surface can be changed in a large range through the combination of the different base functions given above.

III.   Aerodynamic Model

Aerodynamic models are widely used in various kinds of hypersonic aerodynamic shape optimization during the preliminary design due to the high efficiency and reasonable accuracy, such as the Newtonian flow, tangent-cone/wedge, and shock-expansion theory. Among these approximate methods, the tangent-cone method is especially popular and frequently yields very reasonable results when applied to three-dimensional hypersonic slender shapes, which is further improved by Cruz and Sova [32] with higher accuracy. Therefore, the improved tangent-cone method is employed here to approximate the inviscid pressure on the windward surface and the hypersonic expansion-wave relation is used on the leeward surface [33]:

$$p = \begin{cases} 1 + \left(\frac{2\gamma}{\gamma+1}M_\infty^2 \sin^2\beta - \frac{\gamma-1}{\gamma+1}\right) \cdot \left(1 + \frac{\gamma M_\infty(\beta-\theta)^2\cos^2\beta}{1+[(\gamma-1)/2]M_\infty^2\sin^2\beta}\right)^{-1} & (K \geq 0) \\ \left(1 + \frac{\gamma-1}{2}K\right)^{2\gamma/\gamma-1} & \left(-\frac{2}{\gamma-1} < K < 0\right) \\ 0 & \left(K \leq -\frac{2}{\gamma-1}\right) \end{cases} \tag{5}$$

where $p = p_w/p_\infty$, the hypersonic similarity parameter $K = M_\infty\theta$, and θ is the deflection angle of body surface relative to the freestream direction. The shock wave angle β can be approximated as [34]

$$\beta = \frac{\gamma+1}{\gamma-1}\left[1 + \sqrt{1 + \frac{2(\gamma+3)}{(\gamma+1)^2 M_\infty^2 \theta^2}}\right] \cdot \theta \tag{6}$$

One phenomenon that cannot be neglected in hypersonic flow is the strong viscous interactions, which have a significant effect on the pressure distribution of the body surface. Such influence can be captured by the concept of effective shape, namely, the original body plus the boundary-layer displacement thickness. A feasible effective shape determination method was put forward recently in [31] according to a vorticity criterion. However, the method is based on the numerical solutions, which prevents its application to the rapid optimization problem. Therefore, an engineering approach put forward by Bertram [35] is adopted to obtain the boundary-layer displacement thickness rapidly, which was also employed by Anderson et al. [36] in the waverider optimization. The expression is as follows:

$$\frac{d\delta_x^*}{dx} = \frac{\xi}{M_\infty \sqrt{p}}\left(1 + \frac{\xi}{2p}\cdot\frac{dp}{d\xi}\right) \qquad (7)$$

where

$$\xi = 0.425(\gamma-1)\left(\frac{T_w}{T_{ad}} + 0.35\right)\bar{\chi}$$

$$\bar{\chi} = \frac{M_\infty^3}{\sqrt{Re_{x,\infty}}}\sqrt{C_w}$$

$$C_w = \left(\frac{T^*}{T_\infty}\right)^{1/2}\frac{T_\infty + 110.4}{T^* + 110.4} \qquad (8)$$

where the subscripts ∞ and w represent the quantities based on undisturbed freestream conditions and wall conditions, respectively; T_{ad} is the adiabatic wall temperature; and T^* is the reference temperature, which can be approximated using the following expressions [37,38]:

$$\frac{T_{ad}}{T_\infty} = 1 + \sqrt{Pr^*}\cdot\frac{\gamma-1}{2}M_\infty^2 \qquad (9)$$

$$\frac{T^*}{T_\infty} = 1.28 + 0.023M_\infty^2 + 0.58\left(\frac{T_w}{T_\infty} - 1.0\right) \qquad (10)$$

where $Pr^* = 0.72$ and $T_w = 1000$ K are assumed.

The detailed steps for calculating the aerodynamic forces are summarized as follows:

1) Calculate the pressure distribution on the original body surface using Eq. (4).

2) Calculate the viscous interaction parameters $\bar{\chi}$ and ξ by Eqs. (7–9).

3) Combine Eqs. (4) and (6) to obtain an ordinary differential equation about $dp/d\xi$, which is then solved by the fourth-order Runge–Kutta method starting at the leading edge and progressing in the X direction with the initial conditions: $\bar{\chi} = 0$, $p = p_{w,0}/p_\infty$, where $p_{w,0}$ is the pressure calculated in step 1. More detailed solving process is given in [35].

4) The flight altitude studied in this paper is above 40 km. Therefore, a full laminar flow is assumed due to the low Reynolds number. A laminar skin friction formula that can consider the strong viscous interaction effects is employed [37]:

$$C_f = 0.664\sqrt{\frac{p(x)C_w}{Re_{x,\infty}}} \qquad (11)$$

5) The base pressure is approximated by the freestream static pressure.

6) Obtain the final aerodynamic performance by the integration of forces on body surface.

IV. Genetic Algorithm Optimization Framework

GAs perform a global search from a population of individuals by mimicking the process of evolution without depending on the gradient information, which can not only overcome the defect of being liable to obtain the local optimum for some traditional algorithms, but also be easily incorporated into existing frameworks. Therefore, GAs have been used extensively in the problem of aerodynamic shape optimization [39–41]. Here a real-coded-based GA is applied to the quasi-waverider optimization, where the fitness, chromosomes, and genes correspond to the objective function, design candidates, and design variables, respectively. After numerous attempts for achieving rapid convergence and robust optimum results, the parameters listed in Table 2 are employed for the present study.

The GA optimization framework of the quasi-waverider is shown in Fig. 5, where the constraints of volumetric efficiency, trim, and longitudinal static stability are included. Note that, if no constraint is assigned, the program will directly pass the corresponding step to the next one.

Table 2 Parameters used in GA

Population	Generation	pc	pm	a_i $(1 \leq i \leq 10)$	Δa_{max}
30	200	0.8	0.1	$[-y_{te}, y_{te}]$	$\pm 10\%$

Table 3 Comparison of force coefficients at the condition $M_\infty = 15$, $H = 60$ km, $\alpha = 0$ deg

Performance	Coarser grid	Finer grid
$C_L \times 10^{-2}$	2.910	2.914
$C_{D\_wave} \times 10^{-3}$	3.771	3.774
$C_{D\_fric} \times 10^{-3}$	7.557	7.565
X_{cp}	0.6353	0.6351

In addition, the fitness is assigned according to the weight of L/D:

$$\text{fitness}_i = \frac{(L/D)_i}{\sum_{i=1}^{30}(L/D)_i} \qquad (12)$$

The volumetric efficiency is defined as

$$V_{eff} = \frac{V^{2/3}}{S_{upper} + S_{lower}} \qquad (13)$$

V. Computational Fluid Dynamics Solver

A. Numerical Method

A cell-centered finite volume method is employed to solve the three-dimensional compressible Euler or Navier–Stokes (N-S) equations. The AUSM+ spatial discretization scheme is adopted, with an implicit lower–upper symmetric Gauss–Seidel scheme for the temporal integration to accelerate convergence. More details about the CFD solver and its validation at hypersonic conditions can be found in [31,42].

B. Grid Independence Validation

A half-model grid with approximately 600,000 cells is used, shown in Fig. 6. The grid independence study is conducted using a grid with approximately 1,200,000 cells, refined along the streamwise direction on the body. The corresponding force coefficients are listed in Table 3, including the lift coefficient, wave drag coefficient, friction drag coefficient, and the center of pressure. The reference area of the half-model is 1.828 m^2, being equal to the projected area toward the X–Z plane. The laminar flow model is employed. We can see from Table 3 that the results from two grids are very close. Therefore, the coarser grid is used herein to save the computational costs.

VI. Results and Analysis

The current study is focused on the design condition of Mach 15, including the Euler results and N-S results at three typical flight altitudes of 40, 50, and 60 km. Then the optimum quasi-waverider configurations are obtained through the GA optimization framework by incorporating different constraints: 1) no constraint; 2) constraint of volumetric efficiency; 3) constraint of trim and stability. Note that, for the former two problems, the maximum L/D at small angles of attack is taken as the design objective; whereas for the third problem, the maximum L/D for given lift coefficient is pursued due to the trim requirement. In addition, the calculation condition is kept identical to the corresponding design condition of the optimization program.

Before detailed analysis of the results, the aerodynamic model used for this study is first validated in comparison with CFD. Taking the optimum quasi-waverider obtained at $H = 60$ km without constraint (named "QW2," to be introduced later) as an example, Fig. 7 compares the aerodynamic forces calculated by CFD and the
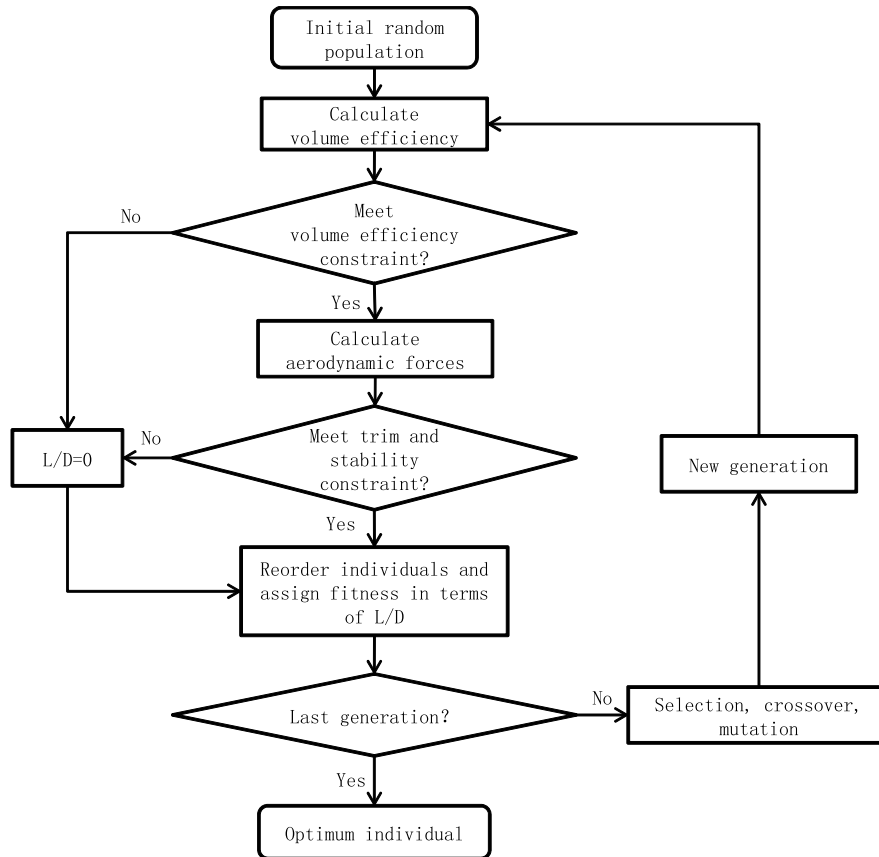
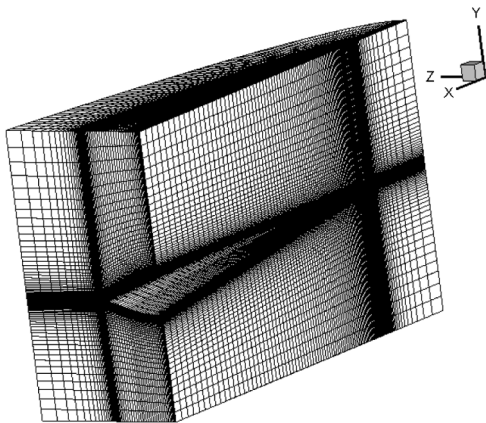Fig. 5   GA optimization framework of the quasi-waverider.

Fig. 6   Half-model grid used in numerical simulations (approximately 600,000 cells).

aerodynamic model (AeroModel) at angles of attack from 0 to 6 deg. Obviously, the results from the efficient aerodynamic model match the CFD data reasonably well at the strong viscous interaction condition, with the maximum relative difference of the lift coefficient, drag coefficient, L/D, and center of pressure being only 3.52, 3.01, 3.71, and 1.06%, respectively.

A.   Optimum Quasi-Waveriders Without Constraint

1.   Inviscid Design Condition

When the viscous effects are not taken into account during the optimization, the maximum L/D at angles of attack from 0 to 4 deg is taken as the design objective. Several comparisons between the generated optimum quasi-waverider (named "QW1") and the original viscous optimized waverider (CW) are shown in Fig. 8, including the profile, L/D, and pressure contour of the flowfield. In Fig. 8a, it can be observed through the curves at the symmetry plane that the

quasi-waverider is slightly thinner than the waverider. According to the result in Fig. 8b, the L/D of the quasi-waverider is even slightly higher than that of the original waverider, with the maximum value being improved from 9.28 to 9.38. The reason can be explained by Fig. 8c, where the pressure contour of the flowfield is compared. It shows that good shock wave attachment along the leading edge of the quasi-waverider is maintained with only a little spillage at cross sections near the base, which proves the rationality of the quasi-waverider design method. In addition, we can also find that the thinner nose of the quasi-waverider leads to a weaker shock wave, making the drag wave lower and L/D higher than those of the original waverider.

2.   Design Condition at Different Altitudes

When the viscous effects at different flight altitudes are considered, the maximum L/D at angles of attack from 0 to 6 deg is taken as the design objective during the optimization. The profile curves at the symmetry plane of optimum quasi-waveriders at different conditions are shown in Fig. 9, where "Inviscid" corresponds to the profile curve of QW1 mentioned above. It shows that different profile curves are close near the end due to the same height constraint and the difference mainly exists near the nose: the deflection angle turns smaller as the flight altitude becomes higher. Such results can be explained by the strong viscous interactions: as the flight altitude increases, the viscous interaction effects become stronger and the boundary-layer displacement thickness becomes thicker, making the shock wave stronger for the same shape. Therefore, in order to weaken the shock wave and correspondingly reduce the wave drag, the deflection angle of the optimum quasi-waverider near the nose tip is smaller at higher altitude.

Comparison of the maximum L/D at different conditions between the original waverider and different optimum quasi-waveriders is shown in Fig. 10. It shows that at each design condition, the optimum quasi-waverider has higher maximum L/D than that of the original waverider. Taking the quasi-waverider optimized at $H = 60$ km (named "QW2") as an example, the comparison of L/D and wave drag coefficient with the original waverider is given in Fig. 11,
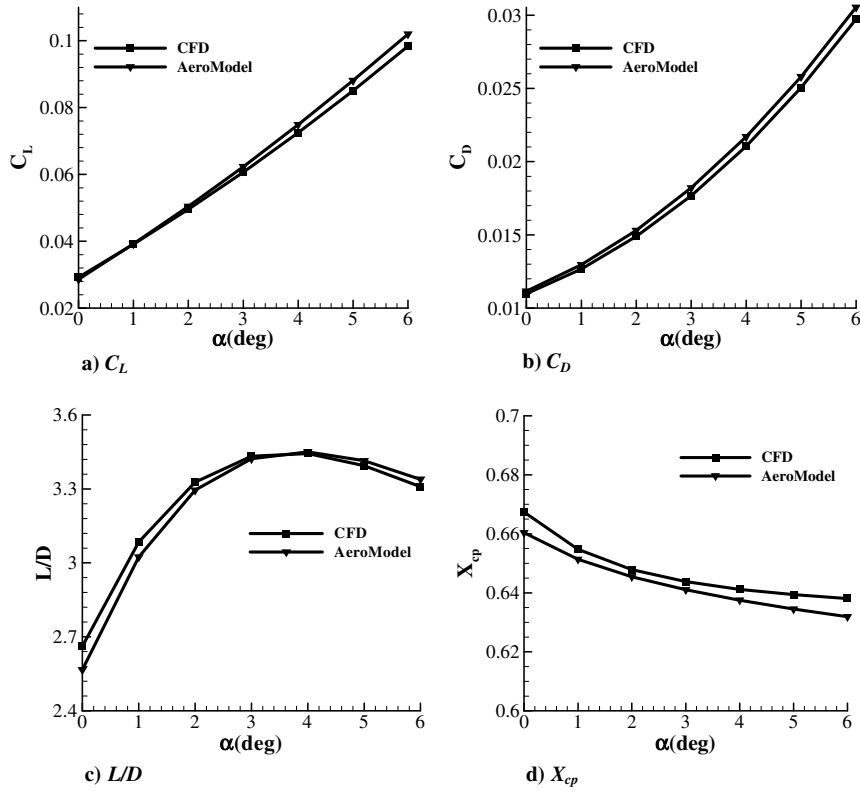
a) C_L

b) C_D

c) L/D

d) X_{cp}

Fig. 7 Comparison of results calculated by CFD and aerodynamic model.

a) Profile

b) L/D

c) Pressure contour of the flowfield at $\alpha=0$ **deg**
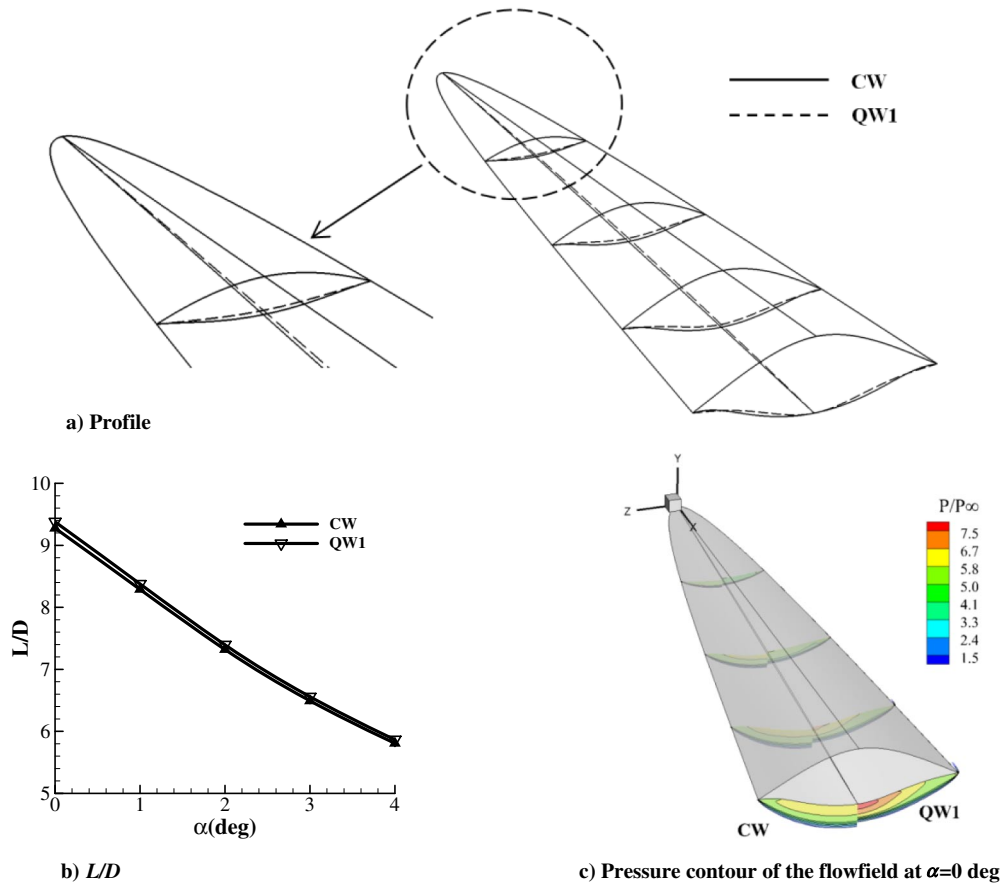
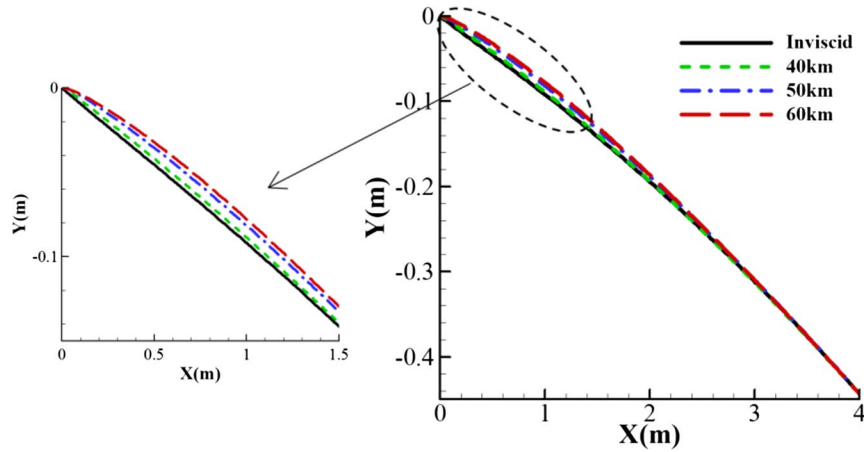**Fig. 8 Comparison of the original waverider and quasi-waverider optimized at the inviscid condition.**

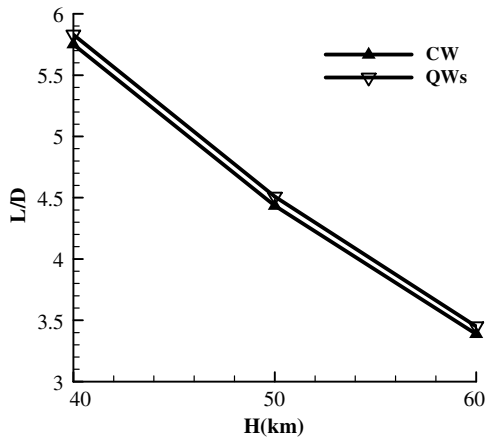**Fig. 9   Comparison of curves at the symmetry plane of optimum quasi-waveriders at different conditions.**

Fig. 10   Comparison of the maximum L/D between the original waverider and different optimum quasi-waverider at different altitudes.

where the abscissa is the lift coefficient. Note that only the wave drag is compared because the friction drag of the two configurations is very close. It is found that, for the same lift coefficient, the L/D of the quasi-waverider is higher mainly due to the lower wave drag. The maximum L/D is improved by 2.07% (from 3.38 to 3.45) and the improvement is larger as the angle of attack increases.

Furthermore, the pressure of the two configurations is compared in Fig. 12, including the pressure contour of the flowfield and the lower surface, and pressure distribution at different cross sections. In Fig. 12a, an apparently weaker shock wave exists around the lower surface of the quasi-waverider, which is similar to what is shown in Fig. 8c. The weaker shock wave results in the lower pressure distribution near the leading edge shown in Figs. 12b and 12c. Therefore, the wave drag of the quasi-waverider is lower than that of the original waverider.
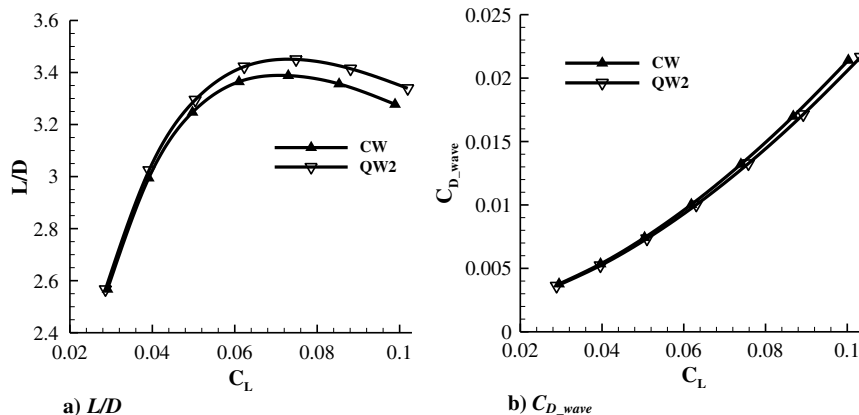
Based on the above results, the optimum quasi-waveriders optimized at different design conditions all have higher maximum L/D compared with the original waverider, which mainly results from the lower wave drag.

B.   Optimum Quasi-Waveriders with Constraint of Volumetric Efficiency

The volumetric efficiency is an indication of the volume relative to the surface area and is often incorporated into waverider optimization program to maintain a balance between usability (high volume) and aerodynamic performance (high L/D) [43]. Although the quasi-waveriders obtained above have higher L/D, their volumetric efficiency is lower than that of the original waverider. For example, the volume efficiency of the configuration QW2 and the waverider is 0.1039 and 0.1165, respectively.

Therefore, the constraint of volumetric efficiency is incorporated into the quasi-waverider optimization. Optimum quasi-waveriders are obtained at four typical design conditions. The maximum L/D of different quasi-waveriders and the original waverider is plotted in Fig. 13. It shows that, as the volumetric efficiency increases, the maximum L/D first increases and then decreases.

The following analysis is focused on the performance of quasi-waveriders with the same volumetric efficiency as the original waverider. The corresponding data are rearranged in Table 5. At the inviscid design condition, the maximum L/D of the quasi-waverider is slightly lower than that of the original waverider; however, when the viscous effects are considered, the maximum L/D of the quasi-waverider is slightly higher, and the advantage is enlarged at higher altitudes. Also taking the quasi-waverider at $H = 60$ km (named "QW3") as an example, Fig. 14 compares the profile and L/D between the two configurations. In fact, only very minor difference exists between the two shapes: the nose region is slightly thinner and the end region is slightly thicker for the quasi-waverider. The geometric feature

a) *L/D*

b) *C_{D_wave}*

Fig. 11   Comparison of aerodynamic performance between the quasi-waverider QW2 and the original waverider at $H = 60$ km.

a) Pressure contour of the flowfield

b) Pressure contour of the lower surface

c) Pressure distribution at different cross sections
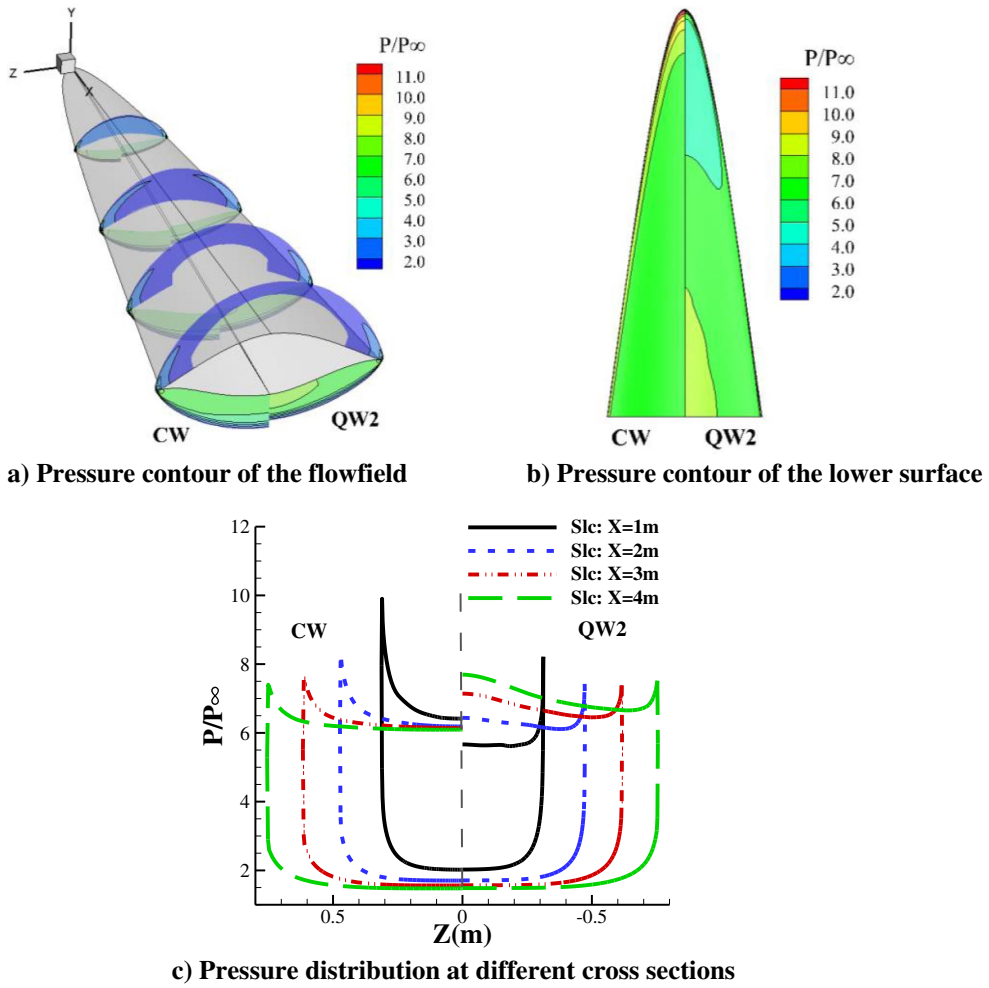
Fig. 12   Comparison of pressure between QW2 and the original waverider at $H = 60$ km, $\alpha = 0$ deg.

a) Inviscid

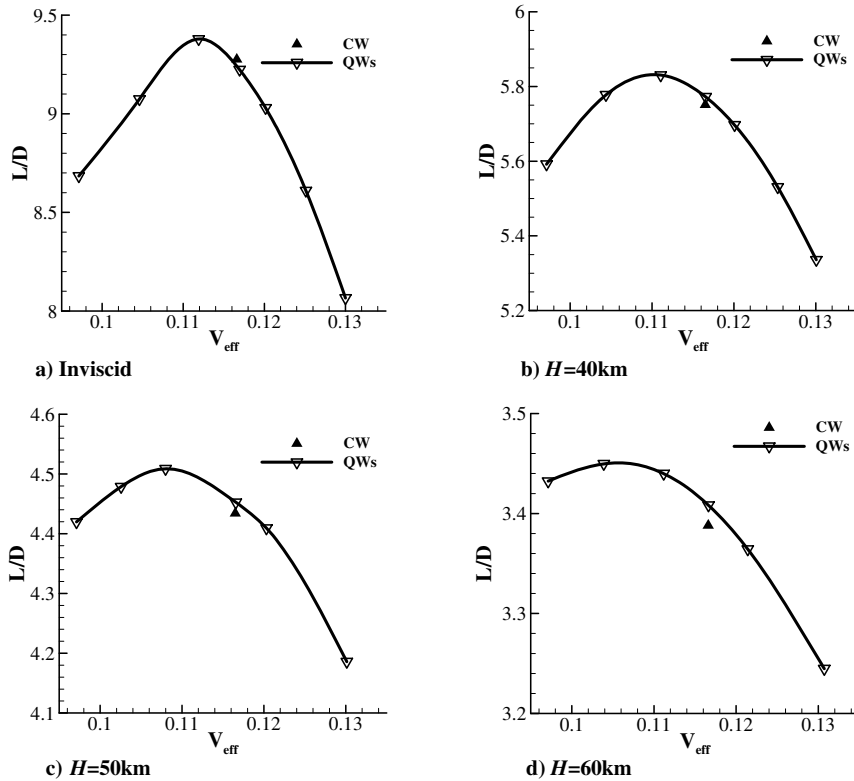
b) H=40km

c) H=50km

d) H=60km

Fig. 13   Maximum L/D of the quasi-waveriders with different volumetric efficiency constraints and the original waverider at different conditions.

Table 4   Maximum L/D of the waverider and quasi-waveriders with the same volumetric efficiency

Design/calculate condition	L/D_CW	L/D_QW	$\Delta L/D$, %
Inviscid	9.28	9.23	−0.54
$H = 40$ km	5.75	5.77	0.35
$H = 50$ km	4.43	4.45	0.45
$H = 60$ km	3.38	3.41	0.89

Table 5   Trim and stability of the waverider at different conditions, $\alpha = 0$ deg

	X_{cp}		X_{ac}		Degree of stability, %	
Condition	Lower	Total	Lower	Total	Lower	Total
Inviscid	0.6223	0.6223	0.6104	0.6107	−0.88	−0.96
$H = 40$ km	0.6157	0.6201	0.6113	0.6107	−0.20	−0.86
$H = 50$ km	0.6102	0.6195	0.6123	0.6108	0.40	−0.77
$H = 60$ km	0.6016	0.6157	0.6142	0.6115	1.48	−0.39

of the thinner nose leads to the lower wave drag and slightly higher L/D.

According to the above results, because the viscous effects (including the impacts of strong viscous interactions and friction drag) are taken into account during the optimization process, the optimum quasi-waverider has minor advantage of L/D over the original waverider even with the same volumetric efficiency at flight conditions of strong viscous interactions.

C.   Optimum Quasi-Waveriders with Constraint of Trim and Stability

Trim and static stability are two key factors that must be considered during the design of any practical vehicle. In order that no extra trim drag is produced by the elevator at the design condition, the constraint of trim is incorporated into the optimization of the quasi-waverider,

which includes two requirements: first, the lift coefficient is specified to balance the weight; second, the center of pressure is coincident with the center of gravity to make the pitching moment be zero. The static stability is evaluated by calculating the difference between the aerodynamic center and the center of gravity (also the center of pressure here). For example, when the degree of stability is asked to be over 1% and the center-of-pressure location is evaluated to be $0.6L$ for the given lift coefficient, the aerodynamic-center location needs to be over $0.61L$. In a word, this is a lift-constrained L/D maximization problem, where the locations of both the center of pressure and the aerodynamic center are constrained. The two parameters are calculated as follows:

$$X_{cp} = \frac{C_{m,\text{nose}}}{C_N}, \qquad X_{ac} = \frac{\partial C_{m,\text{nose}}}{\partial C_L} \qquad (14)$$

where $C_{m,\text{nose}}$ denotes the pitching moment coefficient relative to the nose of the configuration and C_N denotes the normal force coefficient. Note that, referring to the standard convention, a positive pitching moment corresponding to a nose-up moment is ruled here.

First, the characteristic of trim and static stability of the original waverider is analyzed at different design conditions. The variation of the center of pressure with angle of attack at different conditions is shown in Fig. 15, including the lower surface (not integrating the forces of the upper surface) and the total shape. It shows that, for the lower surface, the center of pressure moves forward as the altitude increases at the same angle of attack. This is because the viscous interaction effects are stronger at higher altitudes, which lead to a larger pressure increase near the leading edge, as shown in Fig. 16. However, when the angle of attack increases at the same altitude, the compression effects of the flow around the lower surface turn stronger, tending to weaken the viscous interaction effects. Therefore, at larger angles of attack, the difference of the center of pressure among different conditions is reduced.

The combination of the above two results changes the variation trend of the center of pressure with angle of attack. For the inviscid condition, the center of pressure moves forward as the angle of attack increases, but the trend is just opposite at $H = 60$ km. Such
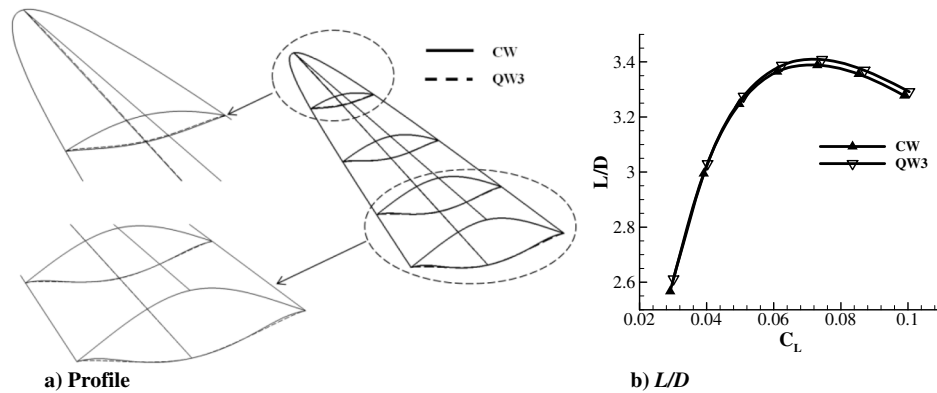

a) Profile   b) *L/D*

Fig. 14   Comparison of profile between the original waverider and QW3 with the same volumetric efficiency at $H = 60$ km.
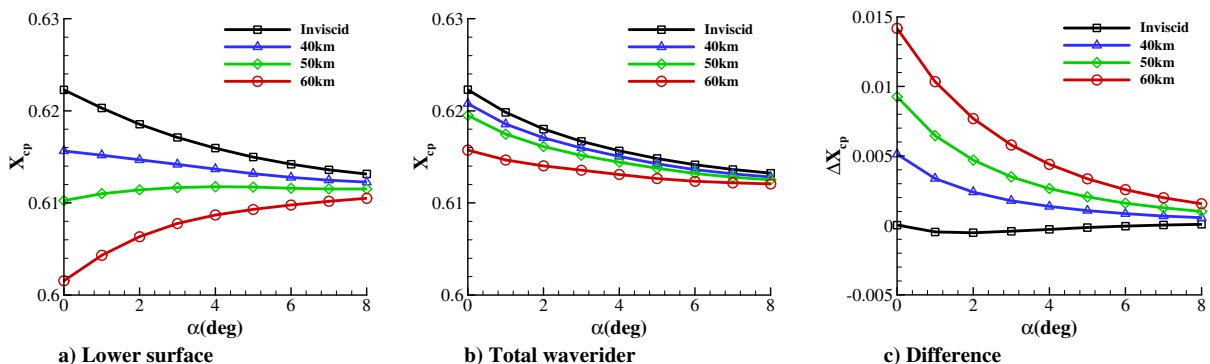

a) Lower surface   b) Total waverider   c) Difference

Fig. 15   Variation of the center of pressure with angle of attack at different conditions.
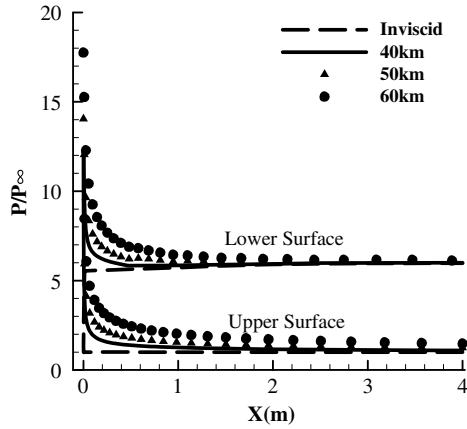
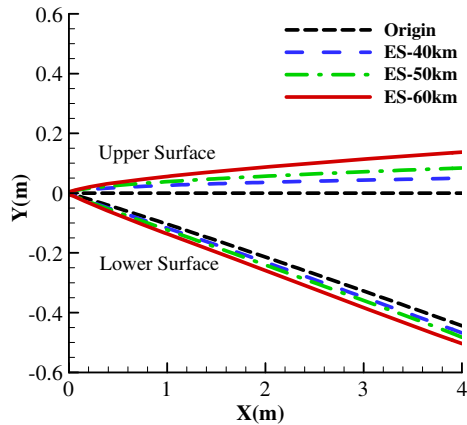Fig. 16   Pressure distribution along the symmetry.

Fig. 17   Original curve and effective shapes along the plane at different conditions, $\alpha = 0$ deg. Symmetry plane at different conditions, $\alpha = 0$ deg.

phenomenon can also be explained directly from the geometric perspective by the variation of the effective shape (ES), which is shown in Fig. 17. Note that the effective shapes here are obtained based on a vorticity criterion and the detailed introduction was given in Ref. [31]. Obviously, as the viscous interaction effects turn stronger, the effective shape changes gradually from a concave surface to a convex one. Then the result is consistent with the conclusion from Ref. [28], which is mentioned earlier in the Sec. I.

However, the variation trend of the center of pressure with angle of attack is different when the upper surface is taken into account, as shown in Fig. 15b. The difference of the center of pressure (ΔX_{cp}) between the total surface and the lower surface is also plotted in Fig. 15c. It can be found that the influence of the aerodynamic force on the upper surface is more and more evident as the altitude increases, which is almost negligible at the inviscid condition. This result is also attributed to the impacts of strong viscous interactions: the pressure near the leading edge of the upper surface is increased, shown in Fig. 16, and thus the center of pressure of the total waverider moves backward.

Furthermore, the center of pressure, the aerodynamic center, and the degree of stability at $\alpha = 0$ deg is listed in Table 5, including the lower surface and the total waverider. Note again that the degree of stability is evaluated by calculating the difference between the aerodynamic center and the center of pressure. It is shown that, although the center of pressure moves forward as the altitude increases, the aerodynamic center moves backward slightly. However, only the lower surfaces at the conditions of $H = 50$ km and $H = 60$ km are statically stable, which is caused by the variation trend of the center of pressure moving backward with angle of attack. In fact, the aerodynamic center varies little with angle of attack. Then taking any angle of attack plotted in Fig. 15 as the design condition, the lower

surface is statically stable because the aerodynamic center is located behind the center of pressure. Nevertheless, the aerodynamic forces on the upper surface reduce the degree of stability, making the total waverider statically unstable.

From the above analysis, we can infer that in order to make the total configuration satisfy the requirement of trim and static stability with the loss of L/D being as low as possible, an optimized lower surface with more convex geometric feature is necessary, which can be realized by the quasi-waverider optimization method.

Here the lift coefficient that corresponds to the maximum L/D of the original waverider is specified at each design condition, which is listed in Table 6. In addition, assume that the center of gravity can be varied along the X axis and the variation range is also given in Table 6.

The profile curves of the optimum quasi-waveriders with different degree-of-stability (ds) constraints are shown in Fig. 18. It is evident that, as the degree of stability increases, the profile curve becomes more and more convex, and consequently the shock wave is detached from the leading edge gradually, which is shown in Fig. 19 (inviscid condition) and Fig. 20 ($H = 60$ km). Note that the pressure increase around the upper surface in Fig. 20 is partly caused by the influence of strong viscous interaction effects.

The aerodynamic performance of the original waverider and optimum quasi-waveriders at the specified lift coefficient of each condition is listed in Table 7. The results from both the aerodynamic model and CFD are listed for further comparison. It can be found that, for some quasi-waveriders, the degree of stability based on CFD results is less than the given constraint of the optimization program, such as the configurations obtained at $H = 40$ km. Apparently, this is caused by the error of the aerodynamic model. However, the difference is generally small, which is especially acceptable in the preliminary aerodynamic design.

Furthermore, based on the CFD results, the L/D variation with degree of stability for the quasi-waveriders is plotted in Fig. 21. Interestingly, the L/D is reduced almost linearly with the increase in degree of stability at each condition, and the corresponding expressions through the least square fitting are also given in Fig. 21. The first-order coefficient of the expression denotes the loss ratio of L/D with degree of stability, and the constant term represents the L/D for the quasi-waverider being critical statically stable. According to the expressions, the L/D of the optimum quasi-waverider with different degree of stability can be estimated easily and rapidly.

Another point deserved to be noted in Fig. 21 is that the slope of the curve, namely, the first-order coefficient of the linear expression, becomes smaller at higher altitude. As mentioned earlier, the higher-altitude condition means the stronger viscous interaction effects, which can be quantified by a widely used viscous interaction parameter $\bar{V}'$, defined as [33]:

$$\bar{V}' = \frac{M_\infty \sqrt{C_w}}{\sqrt{Re_{\infty,L}}} \tag{15}$$

According the Ref. [33], both similarity parameters $\bar{\chi}$ and $\bar{V}'$ govern the laminar viscous interactions. The main difference is that the former parameter governs the induced pressure increment and the latter one governs the pressure coefficient and force coefficients by the viscous interactions. Therefore, the parameter $\bar{V}'$ is used here to discuss the influence of viscous interactions on L/D.

Table 6   Lift coefficient and center-of-gravity range specified during the optimization

Condition	C_L	$\Delta X_{cg}(\Delta X_{\text{cp}})$
Inviscid	0.031	[0.55, 0.65]
$H = 40$ km	0.041	[0.55, 0.65]
$H = 50$ km	0.051	[0.55, 0.65]
$H = 60$ km	0.073	[0.55, 0.65]

a) Inviscid

b) *H*=40km

c) *H*=50km

d) *H*=60km
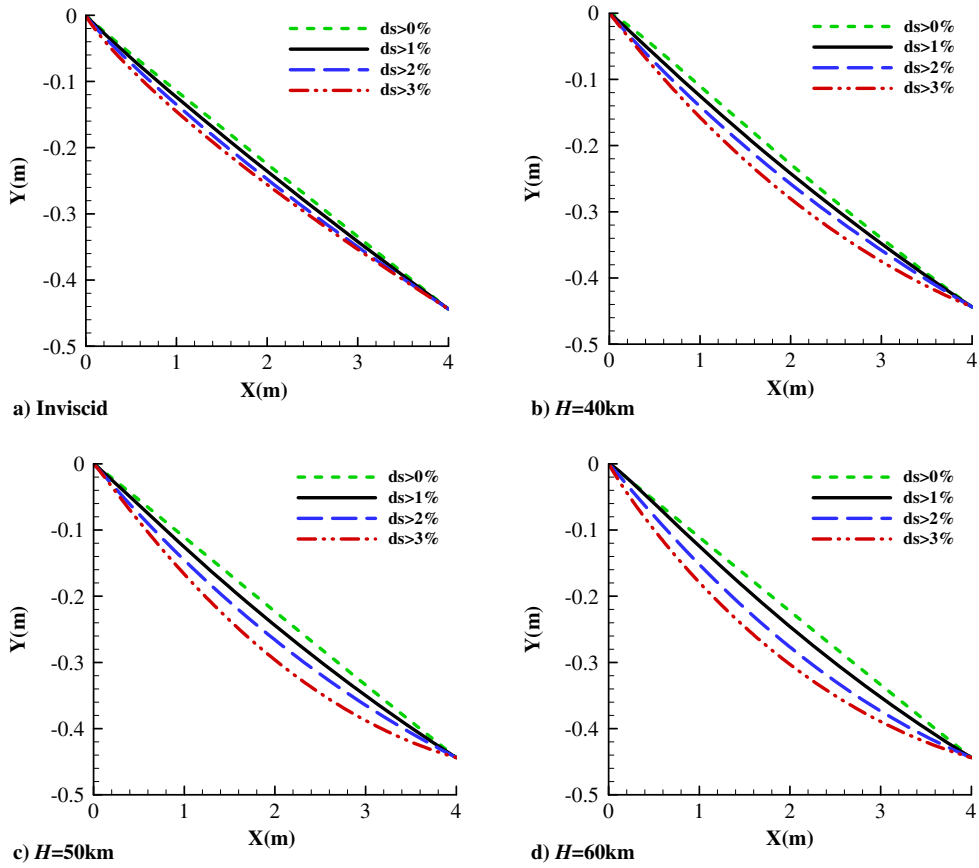
Fig. 18   Comparison of the profile curve with different degree-of-stability constraints.
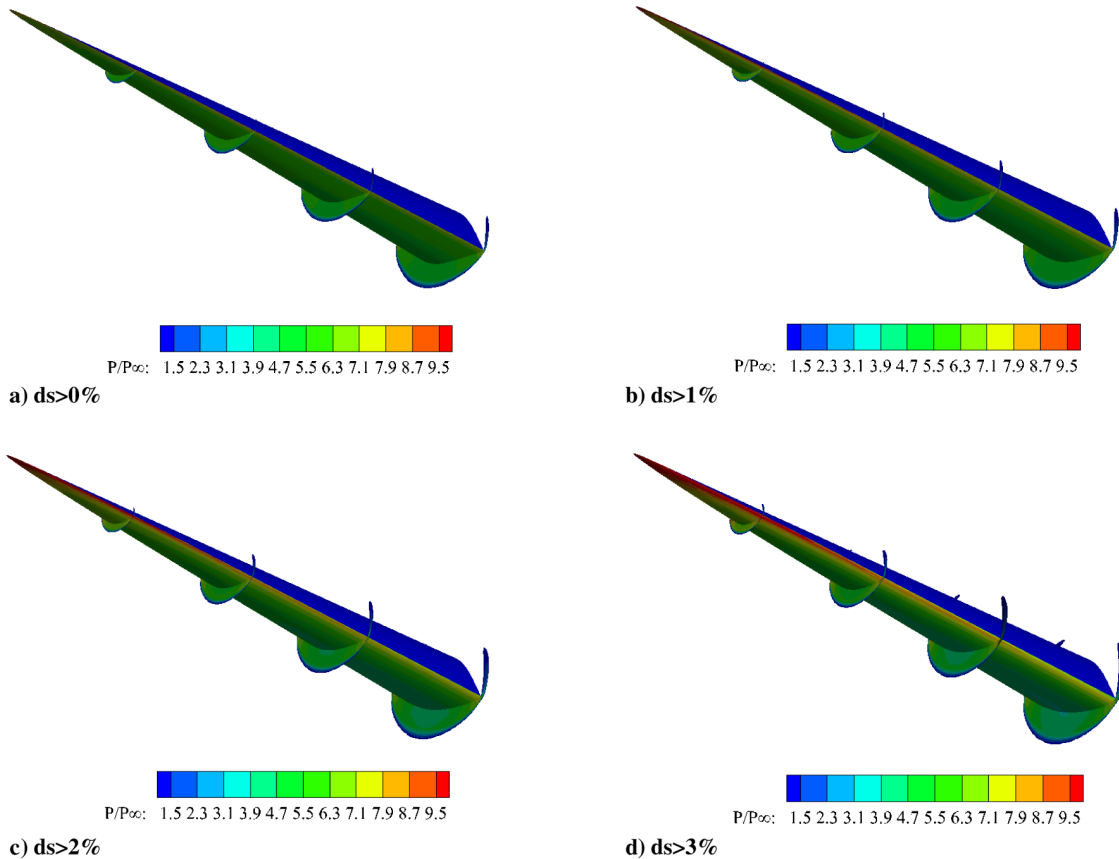

a) ds>0%

b) ds>1%

c) ds>2%

d) ds>3%

Fig. 19   Comparison of flowfield among quasi-waveriders with different degree of stability at the inviscid design condition.
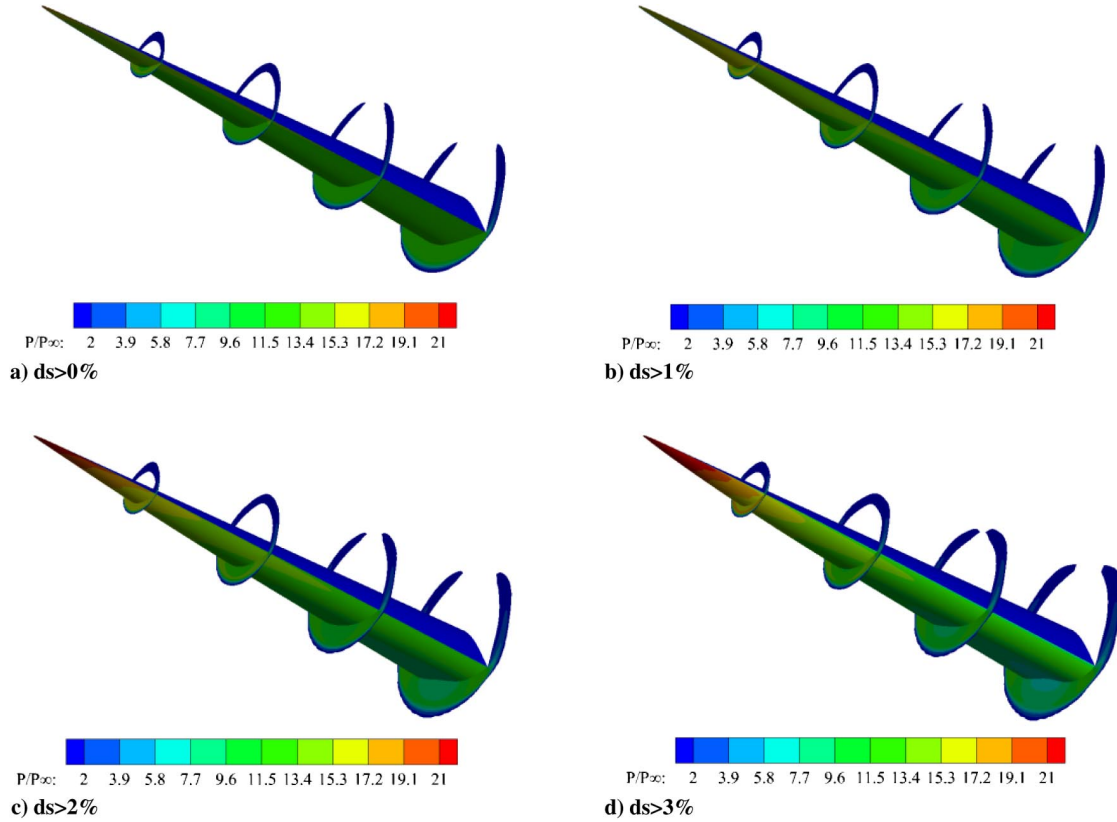
a) ds>0%

b) ds>1%

c) ds>2%

d) ds>3%

Fig. 20 Comparison of flowfield among quasi-waveriders with different degree of stability at $H = 60$ km, $\alpha = 4$ deg.

The values of $\bar{V}'$ at different altitudes are listed in Table 8 and the variation of first-order coefficient, namely, $\partial(L/D)/\partial(ds)$, with $\bar{V}'$ is plotted in Fig. 22. Again an almost linear relationship exists between the two variables. Then the relationship between $\partial(L/D)/\partial(ds)$ and $\bar{V}'$ can be constructed directly:

$$\frac{\partial(L/D)}{\partial(ds)} = 524.5\bar{V}' - 21.82 \qquad (16)$$

According to the above equation, the loss rate of L/D with degree of stability can be easily calculated at different flight conditions, which is useful for the evaluation of the overall performance requirements in the preliminary design. In addition, we should note that Eq. (15) is valid for the degree of stability typically ranging from -0.5 to 3.5%. Larger degree of stability is beyond the optimization target of the current paper in that such requirement may be unnecessary for practical hypersonic vehicles.

Table 7 Aerodynamic performance of the optimum quasi-waveriders with constraints of stability and the original waverider

| Condition	Performance	CW	QW							
			$ds > 0\%$		$ds > 1\%$		$ds > 2\%$		$ds > 3\%$	
			Aero model	CFD	Aero model	CFD	Aero model	CFD	Aero model	CFD
Inviscid	L/D	9.28	8.94	8.99	8.81	8.71	8.58	8.29	8.33	7.86
	X_{cp}	0.6223	0.6126	0.6056	0.5986	0.5905	0.5813	0.5735	0.565	0.5589
	X_{ac}	0.6127	0.6128	0.6063	0.6086	0.6007	0.6014	0.5955	0.595	0.593
	ds, %	−0.96	0.02	0.07	1.00	1.02	2.01	2.20	3.00	3.41
$H = 40$ km	L/D	5.78	5.6	5.68	5.5	5.51	5.33	5.28	5.16	5.02
	X_{cp}	0.618	0.6158	0.6064	0.5983	0.5878	0.5791	0.5696	0.5596	0.5488
	X_{ac}	0.611	0.617	0.6014	0.6083	0.5954	0.5992	0.5895	0.5896	0.5781
	ds, %	−0.70	0.12	−0.50	1.00	0.76	2.01	1.99	3.00	2.93
$H = 50$ km	L/D	4.43	4.31	4.4	4.24	4.29	4.11	4.12	3.98	3.92
	X_{cp}	0.616	0.6146	0.6071	0.598	0.5882	0.5774	0.5681	0.5563	0.5452
	X_{ac}	0.611	0.6165	0.606	0.608	0.5948	0.5974	0.5862	0.5863	0.5725
	ds, %	−0.50	0.19	−0.11	1.00	0.66	2.00	1.81	3.00	2.73
$H = 60$ km	L/D	3.38	3.31	3.37	3.28	3.31	3.17	3.16	3.03	2.99
	X_{cp}	0.613	0.6122	0.6058	0.5994	0.5894	0.5766	0.5678	0.5548	0.5513
	X_{ac}	0.61	0.6132	0.6071	0.6094	0.5956	0.5967	0.5894	0.5848	0.5829
	ds, %	−0.30	0.10	0.13	1.00	0.62	2.01	2.16	3.00	3.16
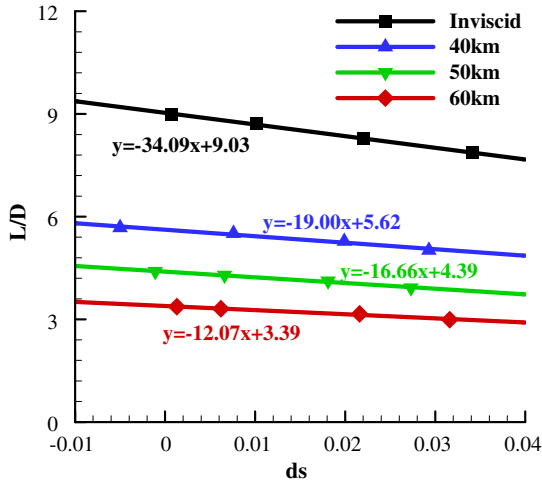
Fig. 21 L/D **variation with degree of stability for quasi-waveriders at different conditions.**

Table 8   Values of the viscous interaction parameter $\bar{V}'$ at different conditions

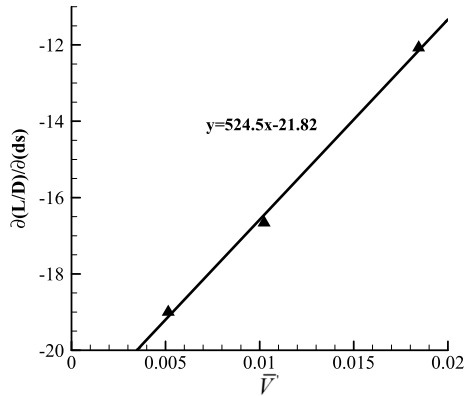| M_∞	H, km	L, m	$\bar{V}' \times 10^{-2}$
15	40	4	0.514
15	50	4	1.023
15	60	4	1.845

Fig. 22   Variation of $\partial(L/D)/\partial(ds)$ with the viscous interaction parameter $\bar{V}'$.

VII.   Conclusions

To improve the longitudinally static stability of the original waveriders with the loss of L/D being as small as possible, a design and optimization method for hypersonic quasi-waverider configuration is presented in this paper. An efficient and accurate aerodynamic model that can consider the impacts of strong viscous interaction effect is employed during the GA optimization process.

When no constraint of volumetric efficiency or stability is given, it is found that the resulting optimum quasi-waveriders have slightly higher L/D than the original waverider due to the lower wave drag. Then optimum quasi-waveriders are obtained based on the constraint of volumetric efficiency. For the optimized quasi-waveriders with the same volumetric efficiency as the original waverider, a minor advantage of L/D also exists at the strong viscous interaction conditions. Finally, constrained by the degree of stability, optimum quasi-waveriders are generated at different design conditions. It is discovered that the L/D is reduced almost linearly with the increase in degree of stability. Furthermore, a linear relationship is also constructed between the variation of L/D with respect to degree of stability and the viscous interaction parameter $\bar{V}'$.

In addition, the results obtained in this paper may also help us to gain more understanding about the connection between the geometric feature and the aerodynamic performance, such as what profile curve determining a configuration with higher L/D at the strong viscous interaction conditions and what profile curve generating a configuration that is statically stable. Such understanding may also be expanded to the design of any other kind of waveriders and even the conventional lifting-body configuration.

Current work is focused on the quasi-waveriders with sharp leading edge. To obtain a more practical hypersonic configuration, future work will try to take into account the influence of blunting effects, payload, and lateral-directional stability during the optimization.

Appendix: Derivation for the Variation Trend of X_{cp}

A two-segment broken line can be used as a simplified model of a streamline, shown in Fig. A1. For a convex streamline, we have $\theta_1 > \theta_2$ and $\delta\theta > 0$. For a concave streamline, the features are just opposite. The length, force, and moment are nondimensionalized by dl, $(1/2)\rho_\infty V_\infty^2 dl$, and $(1/2)\rho_\infty V_\infty^2 dl^2$, respectively.

The dimensionless resultant force parallel to Y axis is

$$F_y^* = C_{p1}\cos\theta_1 + C_{p2}\cos\theta_2 \qquad (A1)$$

where the pressure coefficient is

$$C_p = \frac{p - p_\infty}{(1/2)\rho_\infty V_\infty^2} \qquad (A2)$$

The moment produced by F_y^* is

$$M_{Oy}^* = 0.5C_{p2} \cdot \cos^2\theta_2 - 0.5C_{p1} \cdot \cos^2\theta_1 \qquad (A3)$$

Thus, the dimensionless location of pressure center is

$$X_{cp} = \frac{M_{Oy}^*}{F_y^*} = \frac{0.5C_{p2} \cdot \cos^2\theta_2 - 0.5C_{p1} \cdot \cos^2\theta_1}{C_{p1}\cos\theta_1 + C_{p2}\cos\theta_2} \qquad (A4)$$

The Newtonian theory is adopted here to calculate the pressure coefficient at hypersonic conditions:
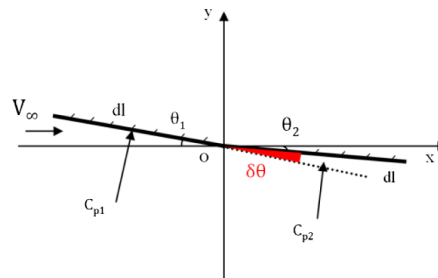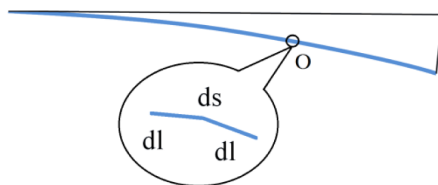

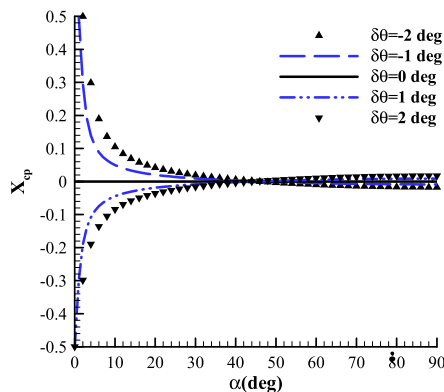**Fig. A1   Simplified model of a streamline.**

Fig. A2   Center-of-pressure variation with angle of attack for different $\delta\theta$.

$$C_p = 2\sin^2\theta \quad (A5)$$

Also note

$$\theta_1 = \theta_2 + \delta\theta \quad (A6)$$

Substituting Eqs. (A5) and (A6) into Eq. (A4), we obtain

$$X_{cp} = \frac{\sin^2\theta_2 \cdot \cos^2\theta_2 - \sin^2(\theta_2 + \delta\theta) \cdot \cos^2(\theta_2 + \delta\theta)}{2\sin^2(\theta_2 + \delta\theta)\cos(\theta_2 + \delta\theta) + 2\sin^2\theta_2\cos\theta_2} \quad (A7)$$

In Fig. A1, if the angle of attack is defined as the angle between the second segment of the broken line and the X axis, we have $\alpha = \theta_2$. Hence, for a given $\delta\theta$, Eq. (A7) depicts the variation of X_{cp} as a function of α. The results are shown in Fig. A2 for different values of $\delta\theta$. We can find that, for a positive value of $\delta\theta$, X_{cp} increases monotonically as angle of attack increases, whereas for a negative value of $\delta\theta$, X_{cp} decreases monotonically as angle of attack increases.

Therefore, from the above analysis we can conclude that, as the angle of attack increases, the center of pressure moves backward for a convex streamline and moves forward for a concave one.

Acknowledgments

References

[1] Whitehead, A., Jr., "NASP Aerodynamics," *AIAA First National Aerospace Plane Conference*, AIAA Paper 1989-5013, July 1989.
[2] Walker, S., "Falcon Hypersonic Technology Overview," *13th AIAA International Space Planes and Hypersonic Systems and Technologies Conference*, AIAA Paper 2005-3253, May 2005.
[3] Dolvin, D., "Hypersonic International Flight Research and Experimentation (HIFiRE) Fundamental Sciences and Technology Development Strategy," *15th AIAA International Space Planes and Hypersonic Systems and Technologies Conference*, AIAA Paper 2008-2581, May 2008.
[4] Kuchemann, D., *The Aerodynamic Design of Aircraft*, Pergamon Press, Oxford, 1978, pp. 448–510.
[5] Nonweiler, T. R. F., "Aerodynamic Problems of Manned Space Vehicles," *Journal of Royal Aeronautical Society*, Vol. 63, No. 585, 1959, pp. 521–528.
https://doi.org/10.1017/S0368393100071662
[6] Bowcutt, K. G., Anderson, J. D., and Capriotti, D., "Viscous Optimized Hypersonic Waveriders," *AIAA 25th Aerospace Sciences Meeting*, AIAA Paper 1987-0272, Jan. 1987.
[7] Corda, S., and Anderson, J. D., "Viscous Optimized Hypersonic Waveriders Designed from Axisymmetric Flowfields," *AIAA 26th Aerospace Sciences Meeting*, AIAA Paper 1988-0369, Jan. 1988.

[8] Sobieczky, H., Dougherty, F. C., and Jones, K., "Hypersonic Waverider Design from Given Shock Waves," *Proceedings of the First International Waverider Symposium*, Univ. of Maryland, College Park, MD, Oct. 1990, pp. 1–18.
[9] Takashima, N., and Lewis, M. J., "Waverider Configurations Based on Non-Axisymmetric Flow Fields for Engine-Airframe Integration," *32nd Aerospace Sciences Meeting and Exhibit*, AIAA Paper 1994-0380, Jan. 1994.
[10] Rodi, P. E., "The Osculating Flowfield Method of Waverider Geometry Generation," *43rd AIAA Aerospace Sciences Meeting and Exhibit*, AIAA Paper 2005-0511, Jan. 2005.
[11] Geng, Y. B., Liu, H., Ding, H. H., and Wang, F. M., "Optimized Design of Waverider Forebody Derived from Asymmetric Near Isentropic Compression Flow Fields," *Journal of Propulsion and Technology*, Vol. 27, No. 5, Oct. 2006, pp. 404–409 (in Chinese).
[12] Lobbia, M. A., and Suzuki, K., "Experimental Investigation of a Mach 3.5 Waverider Designed Using Computational Fluid Dynamics," *AIAA Journal*, Vol. 53, No. 6, 2015, pp. 1590–1601.
https://doi.org/10.2514/1.J053458
[13] Ferguson, F., Dasque, N., and Dhanasar, M., "Waverider Design and Analysis," *20th AIAA International Space Planes and Hypersonic Systems and Technologies Conference*, AIAA Paper 2015-3508, July 2015.
[14] Kontogiannis, K., and Sobester, A., "Efficient Parameterization of Waverider Geometries," *Journal of Aircraft*, Vol. 54, No. 3, 2017, pp. 890–901.
https://doi.org/10.2514/1.C033902
[15] Wang, J. F., Liu, C. Z., Bai, P, Cai, J. S., and Tian, Y., "Design Methodology of the Waverider with a Controllable Planar Shape," *Acta Astronautica*, Vol. 151, June 2018, pp. 504–510.
https://doi.org/10.1016/j.actaastro.2018.06.048
[16] Hu, S. Y., Jiang, C. W., Gao, Z. X., and Lee, C. X., "Combined-Wedge Waverider for Airframe–Propulsion Integration," *AIAA Journal*, Vol. 56, No. 8, June 2018, pp. 3348–3352.
https://doi.org/10.2514/1.J055860
[17] Zhao, Z. T., Huang, W., Yan, B. B., Yan, L., Zhang, T. T., and Moradi, R., "Design and High Speed Aerodynamic Performance Analysis of Vortex Lift Waverider with a Wide-Speed Range," *Acta Astronautica*, Vol. 151, July 2018, pp. 848–863.
https://doi.org/10.1016/j.actaastro.2018.07.034
[18] Hinman, W. S., Johansen, C. T., and Rodi, P. E., "Optimization and Analysis of Hypersonic Leading Edge Geometries," *Aerospace Science and Technology*, Vol. 70, Sept. 2017, pp. 549–558.
https://doi.org/10.1016/j.ast.2017.08.034
[19] Li, S. B., Wang, Z. G., Huang, W., Xu, S. R., and Yan, L., "Aerodynamic Performance Investigation on Waverider with Variable Blunt Radius in Hypersonic Flows," *Acta Astronautica*, Vol. 137, May 2017, pp. 362–372.
https://doi.org/10.1016/j.actaastro.2017.05.001
[20] Starkey, R. P., and Lewis, M. J., "Analytical Off-Design Lift-to-Drag-Ratio Analysis for Hypersonic Waveriders," *Journal of Spacecraft and Rockets*, Vol. 37, No. 5, Sept.–Oct. 2000, pp. 684–691.
https://doi.org/10.2514/2.3618
[21] Takashima, N., and Lewis, M. J., "Optimization of Waverider-Based Hypersonic Cruise Vehicles with Off-Design Considerations," *Journal of Aircraft*, Vol. 36, No. 1, Jan.–Feb. 1999, pp. 235–245.
https://doi.org/10.2514/2.2430
[22] Strohmeyer, D., Eggers, T., and Haupt, M., "Waverider Aerodynamics and Preliminary Design for Two-Stage-to-Orbit Missions, Part 1," *Journal of Spacecraft and Rockets*, Vol. 35, No. 4, July–Aug. 1998, pp. 450–458.
https://doi.org/10.2514/2.3375
[23] Heinze, W., and Bardenhagen, A., "Waverider Aerodynamics and Preliminary Design for Two-Stage-to-Orbit Missions, Part 2," *Journal of Spacecraft and Rockets*, Vol. 35, No. 4, July–Aug. 1998, pp. 459–466.
https://doi.org/10.2514/2.3376
[24] Johnson, D. B., Thomas, R., and Manor, D., "Stability and Control Analysis of a Waverider TSTO Second Stage," *AIAA/NAL-NASDA-ISAS 10th International Space Planes and Hypersonic Systems and Technologies Conference*, AIAA Paper 2001-1834, April 2001.
[25] Smith, T. R., Bowcutt, K. G., Selmon, J. R., and Miranda, L., "HIFiRE 4: A Low-Cost Aerodynamics, Stability, and Control Hypersonic Flight Experiment," *17th AIAA International Space Planes and Hypersonic Systems and Technologies Conference*, AIAA Paper 2011-2275, April 2011.
[26] Bowcutt, K. G., "Physics Drivers of Hypersonic Vehicle Design," *22nd AIAA International Space Planes and Hypersonic Systems and Technologies Conference*, AIAA Paper 2018-5373, Sept. 2018.
[27] Rasmussen, M. L., and He, X. H., "Analysis of Cone-Derived Waverider by Hypersonic Small-Disturbance Theory," *Proceedings of the First International Waverider Symposium*, Univ. of Maryland, College Park, MD, Oct. 1990, pp. 1–6.

[28] Jia, Z. A., Zhang, C. A., Wang, K. M., and Wang, F. M., "Longitudinal Static Stability Analysis of Hypersonic Waveriders," *Scientia Sinica*, Vol. 44, No. 10, March 2014, pp. 1114–1122 (in Chinese).
https://doi.org/10.1360/N092014-00058

[29] Mangin, B., Benay, R., Chanetz, B., and Chpoun, A., "Optimization of Viscous Waveriders Derived from Axisymmetric Power-Law Blunt Body Flows," *Journal of Spacecraft and Rockets*, Vol. 43, No. 5, Sept.–Oct. 2006, pp. 990–998.
https://doi.org/10.2514/1.20079

[30] Wang, X. P., Zhang, C. A., Liu, W., Wang, F. M., and Ye, Z. Y., "Effect of Design Parameters on Longitudinal Static Stability of Power Law Waverider," *Journal of Astronautics*, Vol. 40, No. 8, Aug. 2019, pp. 887–896 (in Chinese).

[31] Liu, W., Zhang, C. A., and Wang, F. M., "Modification of Hypersonic Waveriders by Vorticity-Based Boundary Layer Displacement Thickness Determination Method," *Aerospace Science and Technology*, Vol. 75, Jan. 2018, pp. 200–214.
https://doi.org/10.1016/j.ast.2017.12.020

[32] Cruz, C. I., and Sova, G. J., "Improved Tangent-Cone Method for the Aerodynamic Preliminary Analysis System Version of the Hypersonic Arbitrary-Body Program," NASA TM-4165, 1990.

[33] Anderson, J. D., Jr., *Hypersonic and High-Temperature Gas Dynamics*, 2nd ed., AIAA, Reston, VA, 2006, pp. 301–305.

[34] Qu, Z. H., *Hypersonic Aerodynamics*, Press of National Univ. of Defense Technology, Changsha, China, 2000, pp. 69–70.

[35] Bertram, M. H., "Hypersonic Laminar Viscous Interaction Effects on the Aerodynamics of Two-Dimensional Wedge and Triangular Planform Wings," NASA TN-D-3523, 1966.

[36] Anderson, J. D., Jr., Chang, J., and McLaughlin, T. A., "Hypersonic Waveriders: Effects of Chemically Reacting Flow and Viscous Interaction," *30th Aerospace Sciences Meeting and Exhibit*, AIAA Paper 1992-0302, Jan. 1992.

[37] White, F. M., *Viscous Fluid Flow*, 3rd ed., McGraw–Hill, New York, 2006, p. 517.

[38] David, D. J., and Anderson, J. D., "Reference Temperature Method and Reynolds Analogy for Chemically Reacting Non-Equilibrium Flow-fields," *Journal of Thermophysics and Heat Transfer*, Vol. 8, No. 1, July 1993, pp. 190–192.
https://doi.org/10.2514/3.522

[39] Obayashi, S., and Tsukahara, T., "Comparison of Optimization Algorithms for Aerodynamic Shape Design," *AIAA Journal*, Vol. 35, No. 8, Aug. 1997, pp. 1413–1415.
https://doi.org/10.2514/2.251

[40] Liu, J. L., "Intelligent Genetic Algorithm and Its Application to Aerodynamic Optimization of Airplanes," *AIAA Journal*, Vol. 43, No. 3, March 2005, pp. 530–538.
https://doi.org/10.2514/1.7070

[41] Zhang, Q., Ye, K., Ye, Z. Y., and Zhang, W. W., "Aerodynamic Optimization for Hypersonic Wing Design Based on Local Piston Theory," *Journal of Aircraft*, Vol. 53, No. 4, July–Aug. 2016, pp. 1065–1072.
https://doi.org/10.2514/1.C033381

[42] Liu, W., Zhang, C. A., Han, H. Q., and Wang, F. M., "Local Piston Theory with Viscous Correction and Its Application," *AIAA Journal*, Vol. 55, No. 3, March 2017, pp. 942–954.
https://doi.org/10.2514/1.J055207

[43] Lobbia, M., and Suzuki, K., "Design and Analysis of Payload-Optimized Waveriders," *AIAA/NAL-NASDA-ISAS 10th International Space Planes and Hypersonic Systems and Technologies Conference*, AIAA Paper 2001-1849, April 2001.

C. Wen
Associate Editor